Diverse biosphere influence on carbon and heat in mixed urban Mediterranean landscape revealed by high resolution thermal and optical remote sensing

Nicholas C Parazoo[1], Red Willow Coleman[2], Vineet Yadav[1], E. Natasha Stavros[3], Glynn Hulley[1], Lucy Hutyra[4]

[1] Jet Propulsion Laboratory, California Institute of Technology

[2]Harvey Mudd College, Department of Biology

[3]University of Colorado Boulder

[4]Boston University, Department of Earth & Environment

Corresponding Author:

Nicholas C Parazoo

nicholas.c.parazoo@jpl.nasa.gov

Address:

Jet Propulsion Laboratory

4800 Oak Grove Drive

Mail Stop 200-233

Pasadena, CA 91109

Phone: 818.354.2973

Abstract

A fundamental challenge in verifying urban CO_2 emissions reductions is estimating the biological influence that can confound emission source attribution across heterogeneous and diverse landscapes. Recent work using atmospheric radiocarbon revealed a substantial seasonal influence of the managed urban biosphere on regional carbon budgets in the Los Angeles megacity, but lacked spatially explicit attribution of the diverse biological influences needed for flux quantification and decision making. New high-resolution maps of land cover (0.6 m) and irrigation (30 m) derived from optical and thermal sensors can simultaneously resolve landscape influences related to vegetation type (tree, grass, shrub), land use, and fragmentation needed to accurately quantify biological influences on CO_2 exchange in complex urban environments. We integrate these maps with the Urban Vegetation Photosynthesis and Respiration Model (UrbanVPRM) to quantify spatial and seasonal variability in gross primary production (GPP) across urban and non-urban regions of Southern California Air Basin (SoCAB). Results show that land use and landscape fragmentation have a significant influence on urban GPP and canopy temperature within the water-limited Mediterranean SoCAB climate. Irrigated vegetation accounts for 31% of urban GPP, driven by turfgrass, and is more productive (1.7 vs 0.9 μmol m^{-2} s^{-1}) and cooler (2.2 ± 0.5 K) than non-irrigated vegetation during hot dry summer months. Fragmented landscapes, representing mostly vegetated urban greenspaces, account for 50% of urban GPP. Cooling from irrigation alleviates strong warming along greenspace edges within 100 m of impervious surfaces, and increases GPP by a factor of two, compared to non-irrigated edges. Finally, we note that non-irrigated shrubs are typically more productive than non-irrigated trees and grass, and equally productive as irrigated vegetation. These results imply a potential water savings benefit of urban

shrubs, but more work is needed to understand carbon vs water usage tradeoffs of managed vs unmanaged vegetation.

Introduction

Fossil fuel CO_2 emissions from cities account for 70% of anthropogenic emissions globally (United Nations, 2012). Rapid global urbanization is expected to accelerate emissions growth through doubling of urban populations (2.6 to 5 billion) and tripling of urban areas from 2000 to 2030 (DESA UN, 2015). This growth will have direct global impacts through increased greenhouse has (GHG) forcing and numerous local environmental consequences (Grimm, 2008; Seto et al., 2012; Mishra et al., 2015;). Bottom-up (tallied from fuel consumption information) and top-down (using urban GHG monitoring networks) approaches are improving our ability to verify urban CO_2 emissions reductions in support of mitigation policies (Gately et al., 2015; Fischer et al., 2017; Yadav et al, 2021). However, a common challenge in discerning fossil CO_2 trends is accounting for the biological fluxes within and surrounding urban regions (Hutyra et al., 2014).

Urban biogenic CO_2 fluxes vary across a range of scales. Regional variation occurs seasonally with rainfall and water use (Miller, Lehman et al, 2020) as well as spatially through changes in climate (Yadav et al., 2021). Local variation occurs across heterogeneous and diverse landscapes and land use practices (Coleman et al, 2020a,b). For example, management practices such as irrigation can shift the timing of net carbon uptake (Miller, Lehman et al, 2020), and alter responses to drought (Miller, Alonzo et al., 2020) and temperature (Wetherley et al., 2018), relative to native vegetation. Fragmented landscapes, consisting of patches of vegetation surrounded by impervious surfaces, show differences in biomass accumulation and temperature stress along edge-to-interior gradients in urban and non-urban forests (Reinmann et al., 2020). Urban green space experiments that mimic urban forests show potentially significant influence on carbon sequestration over multiple decades (Strohbach et al., 2012). Despite these important influences, variability in land cover, land use, and fragmentation across the urban matrix presents a formidable challenge for disentangling fossil vs biological influences on urban carbon budgets.

Modeling techniques combining vegetation optical remote sensing with flux towers and machine learning are improving assessments of urban biogenic CO_2 flux and attribution of column CO_2 anomalies across urban-non-urban gradients (Wu et al., 2021). Such techniques account for the influence of sub-grid land cover variations (~0.5 km) on gridded CO_2 flux (~ 5 km), thereby filling gaps left by coarser resolution regional and global models (> 50 km). However, local variations in biogenic carbon flux associated with heterogeneous and diverse urban landscapes, which occur at very high spatial resolution (VHR; < 30 m), present a computational challenge for large scale models. Consequently, our ability to detect and quantify differences in vegetation seasonal phase, stress response, and growth rates across native, managed, and fragmented vegetation is limited.

Here, we leverage new VHR maps of land cover and land use obtained from optical and thermal remote sensing imagery (Coleman et al., 2020a,b) with the Urban Vegetation and Photosynthesis and Respiration Model (UrbanVPRM) to analyze seasonal variations of gross primary production (GPP) as a function of land cover (grass, shrub, tree), land use (irrigated fraction), and landscape fragmentation (edge, interior) across urban and non-urban subregions across the geographically complex Southern California Air Basin (SoCAB) for one year. Our primary objective is to identify dominant landscape effects on the timing and amplitude of seasonal GPP in a water-limited Mediterranean environment. In particular, we provide critical bottom-up context for a recent top-down study (Miller, Lehman et al, 2020) attributing seasonally varying biospheric fluxes in LA to irrigated urban vegetation. We address the following science questions: (1) Is irrigated urban vegetation the dominant driver of GPP in LA as expected from Miller, Lehman et al (2020)? (2)

Is edge vegetation more productive than interior vegetation? (3) How do fragmentation effects differ between temperature and water limited climates? The paper is organized as follows: Section 2 provides an overview of UrbanVPRM and vegetation classification; Section 3 presents maps and seasonal time series of GPP as functions of land cover, irrigation fraction, and fragmentation; Section 4 discusses the dominant drivers of urban and non-urban carbon cycles within SoCAB and their implications; Section 5 summarizes main conclusions.

2 Methods

2.1 Study Region

Our study focuses on seasonal and spatial variations in GPP across SoCAB and the greater metropolitan urban area of Los Angeles (LA) (**Fig 1**) over a one-year period from July 2017 – June 2018. This region is geographically and topographically complex, encompassing an area of ~16,000 km^2 and contains a mixture of topographic features, unmanaged, non-urban vegetation including semi-arid Mediterranean climate, diverse land cover, and heavily managed urban vegetation. The climate is characterized by seasonal changes in rainfall with hot, dry summers and mild, rainy winters.

2.2 UrbanVPRM

We estimated GPP across urban and non-urban SoCAB at 30 m resolution using the Vegetation Photosynthesis and Respiration Model (VPRM), a simplified light-use efficiency carbon model to directly quantify ecosystem carbon fluxes, relying on spatially explicit meteorological forcing and remote-sensing to drive phenology and water stress (Mahadevan et al, 2008). We retain the original formulation of GPP as described in Mahadevan et al (2008),

$$GPP = -\lambda \, x \, T_{scale} \, x \, P_{scale} \, x \, W_{scale} * EVI * \frac{1}{(1 + PAR/PAR_o)}$$

accounting for seasonal variations in light (Photosynthetically Active Radiation, or PAR) and light absorption as determined from Enhanced Vegetation Index (EVI), the variation in optimal light use efficiency (LUE, denoted by λ) across vegetation types, and downregulation of LUE due to temperature stress (T_{scale}), water stress (W_{scale}), and leaf age (P_{scale}). Note that we have replaced gross ecosystem exchange (GEE) in the original formulation with GPP, and multiplied the right side by (-1), such that values are positive definite and represent the increase in carbon in vegetation. The main innovations in this study are the use of new high-resolution inputs including (1) 0.6 m land cover maps to determine fractional vegetation classes within the 30 m VPRM grid, (2) 30 m maps of EVI and Land Surface Water Index (LSWI) from Sentinel-2 harmonized surface reflectance to constrain light absorption, phenology and water stress, and (3) 1.3 km maps of PAR and temperature from the Weather Research Forecasting (WRF) model. We loosely refer to this version of the model as UrbanVPRM following Hardiman et al (2017) since we suppress GPP due to impervious surfaces in our land cover map.

Model parameters including λ and half saturation value of PAR (PAR_o), which determine the sensitivity of GPP to meteorological forcing as a function of vegetation type, are optimized though nonlinear least squares against flux tower observations of CO_2 flux, and assigned to a model grid cell in a look up table approach. GPP parameters are obtained from Park et al (2018) and optimized against net ecosystem exchange CO_2 flux data in non-urban vegetation within SoCAB. FLUXNET sites include Coastal Sage, Grassland, and Oak/Pine forest (http://www.ess.uci.edu/~california), which are used here to parameterize shrub, grass, and tree vegetation, respectively. GPP parameters are assigned to fractional land cover classes (tree, grass, shrub) within each 30 m UrbanVPRM grid cell, derived using existing 0.6 m urban land cover maps obtained from airborne and satellite optical imagery (Section 2.3). Flux measurements in semi-arid urban regions characteristic of SoCAB, which includes a mixture of managed land-cover types (e.g., lawns, parks, gardens), are unavailable at the time of this study. We prescribe non-urban parameters for urban and non-urban landcover classes, and allow remote sensing inputs to control seasonal GPP dynamics across urban gradients.

The strength of UrbanVPRM lies in its remote sensing constraints. Spaceborne remote sensing inputs include Sentinel 2 harmonized reflectance in the red (ρ_{red}, 0.64-0.67 μm), near-infrared (ρ_{NIR}, 0.85-0.88 μm), and shortwave-infrared (ρ_{SWIR}, 1.57-1.65 μm) bands (Claverie et al., 2018), which are used to define EVI ((ρ_{NIR}- ρ_{red})/ρ_{NIR}) and LSWI ((ρ_{NIR}- ρ_{swir})/(ρ_{NIR}+ ρ_{swir})) following Mahadevan et al (2008). EVI is used as a direct input into the GPP model, whereas LSWI is used as an input in the P_{scale} ((1+LSWI)/2) and W_{scale} ((1+LSWI)/(1+$LSWI_{max}$) terms. Sentinel-2 data has relatively high spatial resolution (resampled to 30 m) and frequent revisit time (3-5 days in midlatitudes) making it ideal for studying GPP variability across urban vegetation gradients. Missing EVI and LSWI values, typically from cloud contamination, are gap-filled using linear interpolation between two dates.

Meteorological inputs include hourly PAR and air temperature (T_{air}) obtained from 1.3 km WRF runs from July 2017 when Sentinel 2 data became available to June 2018. The WRF setup and validation procedure are similar to those in Yadav et al (2019, 2021), using the improved hybrid terrain-following vertical coordinate available in WRF v391. MYNN-EDMF boundary layer physics, and scale-aware Grell-Freitas cumulus parameterization. We use a nearest neighbor approach to extract 1.3 km WRF fields across the 30 m UrbanVPRM grid.

Validation of urban GPP is critical but challenging due to (1) unavailable urban flux towers, (2) uncertain GPP partitioning techniques and terrain effects in non-urban flux towers surrounding LA, and (3) lack of equivalent satellite-derived fluxes at 30 m. A recent comparison of urban biogenic CO_2 fluxes at 5 km, including aggregated maps of GPP from the UrbanVPRM configuration described here, and estimates of GPP derived from the Contiguous Solar Induced Fluorescence (CSIF) product (Zhang et al., 2018), showed good agreement of spatial variability over SoCAB from Jul-Sep 2017 (Wu et al., 2021). Given widespread evidence that solar induced chlorophyll fluorescence (SIF) provides an excellent proxy for GPP at 5 km ecosystem scale including California (e.g., Turner et al., 2020 and references therein), we take this analysis one step further by comparing the full annual cycle of UrbanVPRM GPP and CSIF in urban and non-urban SoCAB. This comparison shows similar overall seasonal structure between products (**Fig 2**), including larger magnitude in nonurban regions, and reduced signals in late spring in urban regions (**Fig 2a**). This also shows good agreement of the gradient between urban and nonurban regions, in particular the divergence between regions from Jul-Oct 2017, and increased divergence in Apr 2018 (**Fig 2b**). We explore landcover effects on these patterns in more detail in Section 3.

2.3 Land Cover

Landcover maps are taken from Coleman et al. (2020a), who combined high resolution optical imagery from the Sentinel-2 (10 m) satellite and National Airborne Imagery Program (NAIP, 0.6 m) airborne flights using a random forest algorithm to classify basic vegetated (tree, grass, shrub) and impervious land covers at ~0.6m across the Southern California Air Basin (SoCAB), including the LA megacity. NAIP imagery from 2016 and 2018 are primarily used to classify urban impervious surface area and vegetation (grass, shrub, tree) at 0.6 m native resolution, while Sentinel-2 imagery is used for non-urban vegetation and to remove shadow effects (**Fig 1c**). The technique includes preprocessing for water and shadow effects, selection of training and validation data, and supervised image classification using object-based classification in Google Earth Engine, producing 85% overall accuracy compared to hand-drawn polygons (Coleman et al., 2020a). To preserve land cover heterogeneity in the coarser 30 m UrbanVPRM grid, we use the native 0.6 m classification to derive fractional land cover patches, and assign model parameters and weights accordingly. The 1-2 year time difference between NAIP imagery and UrbanVPRM runs creates a potential mismatch between vegetation class and model inputs, but we assume vegetation change is minimal over this period. We estimate that two-thirds of SoCAB is vegetated (10,700 km^2**; Table 1)**, mostly by shrubs (~50%) surrounding LA, followed by trees (~30%) and grass (~20%). The urban region is dominated by trees and grasses, interwoven with impervious surfaces.

2.4 Irrigated Vegetation

To quantify the impact of irrigation fraction on GPP variability, we use maps of irrigated and non-irrigated vegetation over SoCAB developed by Coleman et al (2020b; **Fig 1d**). The classification leverages diurnal LST acquisitions from cloud-screened images from the ECOsystem Spaceborne Thermal Radiometer Experiment on Space Station (ECOSTRESS; Fisher et al., 2020; Hulley et al., 2021) in the summers of 2018 and 2019, providing information about the strong cooling effect of irrigated vegetation in the afternoon in semi-arid environments. A thermal sharpening algorithm (Hulley 2019a) trained on airborne hyperspectral (AVIRIS) and thermal (HyTES) data and optimized for the LA urban environment (Hulley 2019b) is used to downscale 70 m ECOSTRESS LST to the 30 m UrbanVPRM grid. To unmix impervious surface contributions to thermal data in the 30 m ECOSTRESS pixels, the downscaled LST was multiplied by fractional vegetation derived from the 0.6 m land cover map in Section 2.3 to create a vegetation weighted LST product, which was then used to train a supervised classification model. Analysis of summer morning versus afternoon data in LA shows a more significant difference between afternoon and morning LST in non-irrigated vegetation pixels compared to irrigated pixels, which experience pronounced ET driven afternoon cooling. This afternoon cooling pattern provides the basis for classifying irrigated pixels with 98% accuracy using validation against withheld ECOSTRESS pixels (Coleman, 2020b).

2.5 Fragmented Vegetation

We examine effects of fragmented vegetation on GPP using techniques developed by Reinmann and Hutyra (2017) to distinguish edge from interior vegetation (**Fig 1e**). Our urban-based approach is slightly different from Reinmann and Hutyra (2017), which focused on non-urban areas. We focus only on 30 m^2 pixels composed of at least 75% vegetation (grass, tree, shrub) according to 0.6 m land cover maps (Section 2.3). We then define edge vegetation as any vegetated pixel within 100 m of a non-vegetated surface, which is likely to experience heat island influences from surrounding buildings and impervious surfaces. For larger urban greenspaces, consistent of multiple adjacent vegetated pixels, we define interior vegetation as any non-edge vegetated pixel. Fragmented vegetation accounts for 25% of urban vegetation, and is comprised mainly of edges (80% of fragmented area).

2.6 Analysis

Land cover classification, map production, and regional GPP calculations are performed using Google Earth Engine software. Statistical analyses are performed using MATLAB, using monthly GPP and a subset of randomly selected pixels (100,000 of 20,000,000 total pixels) to mitigate computational burden. We use one-way analysis of variance (*anova1* function in MATLAB) to determine whether monthly mean estimates of GPP across landscape features (e.g, edge tree vs edge grass) are significantly different ($p < 0.05$), and estimate confidence intervals (shaded regions in Figs 3-5) from a modified version of the Tukey-Kramer method for unequal sample sizes (Tukey's honestly significant difference criterion; *multcompare* function in MATLAB). We acknowledge sub-setting leads to representation errors across vegetation classes, and thus inconsistencies with regional values reported in Table 1. While seasonal GPP patterns presented from randomly generated points are broadly consistent with regional patterns, we refer the reader to Table 1 for more accurate regional assessments.

Unless otherwise stated, results are reported for vegetated surfaces, classified as tree, grass or shrub. We present time series of monthly mean GPP per unit area to compare rates of productivity across different regions and vegetation classes, along with temporally and spatially integrated values to illustrate dominant contributions to regional GPP budgets. We do not report results relating to irrigation effects on interior vegetation for specific land cover classes due to insufficient sampling size (< 0.4% of total urban vegetation combined). Finally, we analyze surface temperature differences between vegetation types using two years (2018-19) of ECOSTRESS LST, focusing on the summer average (June-August) across morning-to-afternoon acquisition times. Uncertainty values are presented as standard errors.

3 Results

3.1 Non-urban Vegetation

Regional GPP is subject to strong spatial and seasonal variability driven by topography and heterogenous fragmented landscapes (**Fig 1**). Non-urban vegetation dominates the regional GPP budget, accounting for 80% of annual GPP (4.6 of 5.7 Tg C, **Table 1**). GPP peaks from mid spring (~Apr) to late summer (~Aug), declines rapidly during autumn (Sep-Nov), and gradually recovers into spring (**Fig 2**). This seasonal pattern is driven primarily by non-urban trees and shrubs, which are slightly offset in phasing of peak amplitude (**Fig 3 a and b**). While non-urban trees are the most productive vegetation in SoCAB per unit area in summer, peaking at 7 µmol m^{-2} s^{-1} in June, shrubs are more widespread in the study area (5174 km^2 vs 3378 km^2), peak two months earlier (in April), and sustain high productivity through June. As such, annual integrated GPP across

SoCAB is 50% larger in shrubs (2.9 Tg C) than trees (1.8 Tg C). Non-urban grass is also productive in June, but less widespread. The combination of non-urban shrubs and trees drives a double GPP peak in April and June, respectively.

3.2 Urban Vegetation

Urban vegetation accounts for 20% of annual GPP in SoCAB. This reduced contribution is due to smaller vegetated area (61% of non-urban area) and lower mean annual productivity per vegetated pixel (25% of non-urban GPP). The fractional contribution varies seasonally, peaking at ~30% of SoCAB GPP from Feb-Mar, and decreasing to ~10% from Apr-Aug as mean urban and non-urban GPP rates diverge (**Fig 2a**). Urban vegetation also shows a double GPP peak, but with the first and largest peak occurring earlier (Feb-Apr) with similar contributions from all vegetation types, and a later and secondary summer peak (Jun-Aug) driven mainly by trees and grass (**Fig 3d**). Mean GPP rates are consistent across urban vegetation types with more prominent grass influence, especially in summer, compared to non-urban vegetation (**Fig 3c**). We investigate this contrast in seasonal phasing between non-urban and urban vegetation, and urban shift from spring shrub dominance to summer grass dominance, in more detail below.

3.3 Irrigation and Landscape Fragmentation

We estimate that irrigated vegetation accounts for 11% of vegetated SoCAB landcover and 24% of vegetated urban cover (**Table 1**), and is comprised mainly of turf grass in residential areas and golf courses.

Irrigated vegetation accounts for 21% of vegetated urban area and 31% of urban GPP, but is twice as productive as non-irrigated vegetation (**Fig 4 a-b**). In particular, irrigated GPP increases from the cool wet spring into the hot dry summer, while non-irrigated GPP declines. Both classes decline rapidly in autumn. Fragmented vegetation accounts for 25% of vegetated urban area and 50% of urban GPP. Edge and interior vegetation are equally productive on average (**Fig 4 c-d**), but edge vegetation occupies five times as much area, thus accounting for 83% of the fragmented GPP and 42% of total urban GPP. Irrigated edge vegetation accounts for only 4% of vegetated urban area and 10% of urban GPP, but represents the most productive form of vegetation, peaking at ~4 umol m^{-2} s^{-1} in summer (**Fig 4 e-f**).

Partitioning by vegetation class reveals a more significant effect of irrigation and fragmentation on seasonal GPP (**Fig 5**). Irrigation amplifies grass GPP by two- to three-fold in spring and summer, and doubles shrub GPP in summer (**Fig 5 a-b**). Interior vegetation supports higher tree and grass including 50% higher GPP in summer (**Fig 5c-d**). Irrigation increases edge grass and shrub GPP by 2-fold on average, with increasingly beneficial effects as conditions dry from spring through autumn (e.g., factor of 1.5 vs 3 increase in spring and autumn, respectively; **Fig 5e-f**).

Irrigation and fragmentation also have a significant effect on land surface temperature. In summer, irrigated urban vegetation is 1.8 ± 0.5 K cooler than non-irrigated vegetation on average, and interior vegetation is 1.9 ± 0.9 K cooler than edge vegetation. These effects are strongly dependent on vegetation type, with strongest interior cooling in trees (6.4 ± 1.3) and irrigation cooling in grasses (3.2 ± 1.6). Moreover, the cooling effect of irrigation is enhanced in edge vegetation (4.0 ± 0.9 K), and greatest in irrigated edge grass, which is 4.7 ± 1.2 K cooler on average than non-irrigated edge grass. These cooling effects are significant given the predominance of edge vegetation in our study, which encompasses an area five times greater than that of interior vegetation in urban LA.

3.4 Regional Scaling

Regional estimates of GPP for SoCAB and its urban sub-region are provided in **Table 1**. Irrigation has a significant effect on the mean GPP of urban vegetation, driving a 2-fold increase in the annual mean, including a significant effect during peak heat stress in summer and autumn. What irrigated urban vegetation lacks in spatial extent (21% of urban area), it makes up for in total production (0.36 Tg C, or 31% of total annual urban GPP, 1.15 Tg C). Edges are also a small fraction of urban area (24%), but account for nearly half (42%) of total urban GPP (0.48 Tg C).

4 Discussion

Our main findings support top-down evidence from atmospheric radiocarbon; namely, that the managed urban biosphere contributes significantly to the regional GPP budget of SoCAB, especially during peak water use in summer (Miller, Lehman et al., 2020). Critically, our satellite-constrained, very-high resolution, bottom-up model provides unprecedented, spatially explicit detail on the underlying processes and function of the urban and non-urban biosphere.

Non-urban vegetation (surrounding LA) is strongly seasonal and primarily climate-driven, with sustained high GPP from late spring through late summer (Apr-Aug) and sharp decline in autumn, consistent with winter precipitation, cooler summer temperature, and warm/dry autumn conditions. Seasonal GPP is driven by shrubs in late spring following winter rainfall and favorable temperatures, and trees in mid-summer. Trees are the dominant non-urban vegetation type in terms of mean annual GPP, while shrubs contribute more to regionally integrated GPP across SoCAB due to higher areal coverage (**Table 1** and **Fig 3**).

Los Angeles urban vegetation features prominent double peaks, driven by a mixture of climate (temperature and water stress) and land surface (plant functional type, irrigation, and landscape fragmentation) effects. An early season primary peak spans mid-winter to early spring during peak rainfall, and secondary peak spans warm and dry summer months. The three vegetation classes analyzed in this study (tree, shrub, grass) show similar seasonal patterns, with shrubs and grass outproducing trees by a factor of 2 on average.

In general, irrigation represents a small (14%), but highly productive fraction of urban land use,. Moreover, peak GPP of irrigated vegetation occurs in the dry and hot summer months (**Fig 4a**), when plants are exposed to increased heat and water stress typical of the SoCAB Mediterranean climate, and is three times more productive than non-irrigated vegetation. Overall, irrigated vegetation accounts for 31% of urban GPP and 6% of SoCAB GPP. Importantly, the effect of irrigation is highly land cover dependent, such that the partitioning of GPP between irrigated and non-irrigated land use components can differ significantly. In particular, while grass and shrubs show similar mean GPP and seasonality (**Fig 3C**), non-irrigated shrubs outproduce non-irrigated grass by a factor of 1.5-2 over the entire growing season (**Fig 4b**). Moreover, irrigation has very little impact on shrubs, but increases the GPP of grass by a factor of 2. We attribute the year-round irrigation effect in grass to watering of turfgrass (e.g., lawns and golf courses), and dominance of non-irrigated shrubs in summer to acclimation of native vegetation to the semi-arid Mediterranean climate.

Landscape fragmentation also plays an important role in the urban GPP budget. For example, interior urban trees and turf grass show a slight boost to GPP in summer (**Fig 5d**). We attribute this pattern to reduced heat stress of cooler interior canopies, relative to warmer edge vegetation. with evidence from ECOSTRESS LST data supporting a warming effect on edge vegetation in Los Angeles, especially in grass (+4.7 K). We attribute lower interior LST to a combination of reduced exposure to heat re-radiated from nearby buildings and paved surfaces (e.g., Wetherley et al., 2018), and healthy unstressed vegetation, which is more likely to photosynthesize and self-cool through evapotranspiration. Several recent efforts analyzing diurnal LST change in global urban vegetation canopies find a significant cooling effect of increased green area fraction on daytime LST (Dewan et al., 2021; Du et al., 2019; Vo et al., 2021). Our results suggest that urban planning efforts to alleviate warming trends associated with Urban Heat Islands (UHIs) through increased vegetation coverage (e.g., Chakroborty et al., 2019) should also carefully consider the effect of greenspace interior to edge ratio. In other words, do strategies focused on fewer but larger greenspaces with high relative interior area offer higher cooling potential than those focused on more abundant but smaller greenspaces with higher relative edge area?

Moreover, our results contrast with landscape fragmentation effects in non-urban Massachusetts, with forest growth and biomass increasing from interior to edge, most likely driven by increased light availability near forest edges (Reinmann et al., 2017; 2020). We attribute these contrasting patterns to differences in heat stress, driven by UHIs, and exacerbated hot, dry semi-arid regions such as LA. Indeed, Reinmann et al (2017) find that warmer edges have a negative influence on vegetation growth in the growing season during heat stress periods in the New England. However, increased water availability through irrigation of urban edge vegetation during dry and hot summer months reduces LST by 4.0 K on average and increases edge GPP by a factor of 2. The situation is reminiscent of wet tropical forests, which can maintain or even increase productivity during the dry season through access to subsurface water, despite dry season warming (Guan et al., 2015; Doughty et al., 2019).

Our results indicate that management of the urban biosphere through irrigated vegetation has potential to mitigate UHI effects through the cooling effect of transpiration. This is especially important for edge vegetation, which covers five times as much urban surface area as interior vegetation (Table 1). We note the true extent of edge vegetation is likely higher than estimated in the study, due to our requirement of high vegetation fraction (>75%) in a highly mixed landscape, suggesting increased potential for UHI mitigation.

Irrigated edges also offer an important boost to mean GPP, which is more than double that of non-irrigated edges. While irrigated edges represent the most productive component of the urban biosphere, the total GPP (0.16 Tg C) is small compared to regionally integrated urban GPP (1.15 Tg C) and negligible compared to urban fossil fuel emission (~45 Tg C yr-1; Miller, Lehman et al., 2020) due to its small spatial extent (160 km^2 of 4114 km^2). While there is potential to increase the area of irrigated edged through conversion of non-irrigated edges, the impact on biomass growth, and net carbon exchange, remains to be seen. Moreover, achieving such benefits requires effective irrigation and maintenance practices to slow the rate of vegetation growth and reduce mortality risk, and practices that minimize indirect carbon costs associated with water transport and pruning (Petri et al., 2016; Smith et al., 2019). Specifically, transporting water for irrigation requires energy and fossil fuel emissions, which is likely to offset any carbon uptake savings of vegetation growth.

The dominance of non-irrigated shrubs in the urban GPP budget relative to non-irrigated grass, and nearly equal productivity relative to irrigated grass, suggests that drought tolerant landscaping could provide a strategy to maintain high productivity without the indirect, water usage and energy costs of irrigation. For example, deep rooted native evergreen species such as chaparall are better adapted to maintain metabolism during drought than shallow rooted drought-deciduous species such as coastal sage scrub (e.g., Barbour and Major, 1977).

Urban GPP sensitivity to land cover, land use, and fragmentation, combined with spatial heterogeneity across the urban matrix, and dependence on season and region, presents a formidable challenge for top-down attribution studies of fossil fuel emissions. The methods and results described in this paper demonstrate the potential for leveraging very high resolution optical and thermal remote sensing constraints to refine spatial variability and account for diverse vegetation sensitivities to temperature and water. Our modeling system is capable of identifying and quantifying carbon fluxes at 30 m spatial resolution commensurate with land cover and land use planning, especially in urban regions where ground observations may be limited. Such a method is scalable to global urban regions, and can help address geographical and international differences in climate, land cover, land use, and urban expansion, and better elucidate the role of urban areas in global carbon budgets.

Validation of model results in mixed urban environments is challenging due to lack of (1) urban tower and *in situ* measurements and (2) independent remote sensing measurements of vegetation photosynthesis at scales fine enough to resolve vegetation gradients. We have evaluated model performance at regional scale across urban and non-urban regions within SoCAB through comparison against the CSIF fluorescence product (Zhang et al., 2018), which provides independent and well documented measure of photosynthesis at 5 km scale, and its spatial and temporal variability (**Fig 2**). We find similar seasonal patterns, including (1) reduced productivity in winter and gradual increase through spring, (2) higher productivity in non-urban regions relative to urban regions, and (3) increased divergence between regions from winter to spring (~April). We attribute mismatches including higher loss of urban GPP in November and the stronger contrast between urban and non-urban regions in UrbanVPRM to several uncertainties related to model inputs, process representation, land cover classification, and parameter calibration.

For example, satellite derived land surface water index (LSWI) utilizes shortwave infrared radiation from 1.57-1.65 µm (SWIR1) to capture the effects of water stress in phenological (P_{scale}) and water stress (W_{scale}) downregulation terms as recommended by Mahadevan et al (2008).

However, SWIR in the longer wavelength band (e.g., 2.11-2.29 μm, SWIR2) has been hypothesized to have better performance in characterizing soil water stress and reduced interference from clouds compared to SWIR1 (Kim 2004; Chandrasekar, 2010). We also note that LSWI is not as effective in forested vegetation as in ecosystems that senesce during dry periods, such as grasslands and shrubs characteristic of SoCAB. It could be more effective to also account for changes in atmospheric demand on forest water stress using vapor pressure deficit (Madani et al., 2021), similar to GPP algorithms leveraged by the NASA Soil Moisture Active Passive Level 4 Carbon (SMAP-L4C) and Moderate Resolution Imaging Spectrometer (MOD17) products (e.g., Madani et al., 2017). It is also recommended to use surface temperature (LST) in place of air temperature (T_{air}) to study UHI impacts on GPP, which is found to be more responsive to vegetative cooling in the daytime over global cities (Du et al., 2021)

A more fundamental shortcoming pertains to our model parameters: While GPP spatiotemporal variability is mainly constrained by remote sensing and meteorological data, functional parameters controlling GPP sensitivity to temperature and sunlight (λ and PAR_o) rely on limited non-urban flux towers (Park et al., 2018). This affects seasonal and spatial GPP gradients in urban regions and total GPP relative to non-urban regions in two key ways: (1) high elevation non-urban vegetation is subject to less heat stress than low elevation urban vegetation, which can experience difference sensitivities to heat stress; and (2) irrigated vegetation is likely to have higher tolerance to heat than non-irrigated vegetation. Both problems can be alleviated using more representative flux tower data in irrigated and non-irrigated urban regions, which weren't available at the time of this study.

Moreover, we do not distinguish between evergreen and deciduous species, and instead classify all trees as deciduous in P_{scale}, such that phenological stages (budburst, full canopy, and senescence) are inadvertently applied to evergreens. This provides a possible explanation for the rapid divergence of non-urban GPP in spring, assuming most non-urban trees are evergreen but treated as deciduous. As such, future efforts should pay close attention to plant functional differences such as phenology.

We acknowledge several additional uncertainties in our land cover analysis. First, while our land cover classification algorithm is broadly consistent with dominant vegetation classes in SoCAB based on manual validation (Coleman et al, 2020a), reliance on optical data and low-temporal resolution airborne snapshots (NAIP) excludes information about (1) seasonal vegetation change, which can indicate plant phenological differences; (2) interannual variability that indicates changes in plant structure and function; (3) vegetation height or biomass (from LIDAR) that can indicate maturity, carbon storage capacity, rooting depth, and drought tolerance (e.g., Stovall et al., 2019); or (4) species diversity using functional and structural trait information (Wang et al. 2020; Schneider et al. 2017) that could indicate likelihoods of key native and/or managed species. For example, AVIRIS flights provide functional information about native versus non-native species (Underwood et al. 2007, Wetherley et al., 2018) and adaptation to drought (Miller, Alonzo et al., 2020). Such information could distinguish seasonal drought responses in deeply-rooted Chaparral shrubs versus shallow-rooted Coastal Sage Shrub. Likewise, land use and irrigation classification does not account for year-to-year changes in irrigation, for example related to changes in rainfall or water use restrictions, and the 30-m product used here shows increased uncertainty along vegetation boundaries, especially along the boundary between adjacent land covers (Coleman et al., 2020b).

Taking the above steps to refine land cover and land use classification, model inputs and parameters, and account for interannual variability, will establish more accurate links between climate, land use, and carbon. More accurate GPP assessments with respect to changing climate and land use can inform management practices, provide actionable information to government entities to evaluate and guide progress on attaining emissions goal (Decola et al., 2019) and determine the social and economic benefits of UHI mitigation (Harlan, 2006; Hulley, 2019b).

5 Conclusions

We use remote sensing constraints with an urban land surface model to quantify spatial and seasonal GPP variability across SoCAB at 30 m. The combination of high spatial resolution and optical and thermal remote sensing provides attribution of landscape influences related to vegetation type, landscape fragmentation and irrigation across urban and non-urban gradients. Non-urban vegetation accounts for 80% of the carbon budget of SoCAB. Irrigated urban vegetation, dominated by turf grass, accounts for 37% or urban GPP, and is three times more productive than non-irrigated vegetation during dry and hot summer months. Landscape fragmentation also plays an important role in the urban carbon budget, with cooler interior vegetation supporting increased GPP in spring and summer, and irrigation mitigating stress effects in edge vegetation. Our results support previous findings, and offers a generalized framework to account for mixed land cover effects in global cities.

6 Acknowledgements

The research was carried out at the Jet Propulsion Laboratory, California Institute of Technology, under a contract with the National Aeronautics and Space Administration (80NM0018D0004). Support from the Earth Science Division OCOST program is acknowledged.

7 References

Chakraborty, T. and Lee, X., 2019. A simplified urban-extent algorithm to characterize surface urban heat islands on a global scale and examine vegetation control on their spatiotemporal variability. *International Journal of Applied Earth Observation and Geoinformation*, *74*, pp.269-280.

Claverie, M., Ju, J., Masek, J. G., Dungan, J. L., Vermote, E. F., Roger, J.-C., Skakun, S. V., & Justice, C., 2018: The Harmonized Landsat and Sentinel-2 surface reflectance data set. *Remote Sensing of Environment*, 219, 145-161.

Coleman, R. W., N. Stavros, V. Yadav, N. C. Parazoo, 2020a: A Simplified Framework for High-Resolution Urban Vegetation Classification with Optical Imagery in the Los Angeles Megacity, *Remote Sensing*, 12 (15), p. 2399.

Coleman, R.W., Stavros, N., Hulley, G. and Parazoo, N., 2020b: Comparison of Thermal Infrared-Derived Maps of Irrigated and Non-Irrigated Vegetation in Urban and Non-Urban Areas of Southern California. *Remote Sensing*, *12*(24), p.4102

DeCola, P., & Secretariat, W. M. O., 2017: An integrated global greenhouse gas information system (IG3IS). *WMO Bulletin*, *66*, 38-45

DESA UN, 2015. World Population Prospects: The 2015 Revision, Key Findings and Advance Tables. United Nations, Department of Economic and Social Affairs, New York, Working Paper No. ESA/P/WP.241.

Dewan, A., Kiselev, G. and Botje, D., 2021. Diurnal and seasonal trends and associated determinants of surface urban heat islands in large Bangladesh cities. *Applied Geography*, *135*, p.102533.

Doughty, R., Köhler, P., Frankenberg, C., Magney, T. S., Xiao, X., Qin, Y., … Moore, B., 2019: TROPOMI reveals dry-season increase of solar-induced chlorophyll fluorescence in the Amazon forest. *Proceedings of the National Academy of Sciences*, *116*(44), 22393–22398.

Du, H., Zhan, W., Liu, Z., Li, J., Li, L., Lai, J., Miao, S., Huang, F., Wang, C., Wang, C. and Fu, H., 2021. Simultaneous investigation of surface and canopy urban heat islands over global cities. *ISPRS Journal of Photogrammetry and Remote Sensing*, *181*, pp.67-83.

Fischer, M. L., Parazoo, N., Brophy, K., Cui, X., Jeong, S., Liu, J., … Graven, H., 2017: Simulating estimation of California fossil fuel and biosphere carbon dioxide exchanges combining in situ tower and satellite column observations. *Journal of Geophysical Research*, *122*(6).

Fisher et al. 2020: ECOSTRESS: NASA's Next Generation Mission to Measure Evapotranspiration From the International Space Station. *Water Resources Research, 56*

Gately, C. K., Hutyra, L. R., & Wing, I. S., 2015: Cities, traffic, and CO2: A multidecadal assessment of trends, drivers, and scaling relationships. *Proceedings of the National Academy of Sciences*, *112*(16), 4999–5004.

Grimm, N.B., Faeth, S.H., Golubiewski, N.E., Redman, C.L., Wu, J., Bai, X. and Briggs, J.M., 2008: Global change and the ecology of cities. *Science*, *319*(5864), pp.756-760.

Guan, K., Pan, M., Li, H., Wolf, A., Wu, J., Medvigy, D., … Lyapustin, A. I. 2015: Photosynthetic seasonality of global tropical forests constrained by hydroclimate. *Nature Geoscience*, *8*(4), 284–289.

Hardiman, B. S., Wang, J. A., Hutyra, L. R., Gately, C. K., Getson, J. M. and Friedl, M. A., 2017: Accounting for urban biogenic fluxes in regional carbon budgets, *Sci. Total Environ.*, 592, 366–372.

Harlan, S.L., Brazel, A.J., Prashad, L., Stefanov, W.L., & Larsen, L., 2006: Neighborhood microclimates and vulnerability to heat stress. *Social Science & Medicine, 63*, 2847-2863

Heady, H. F., Barbour, M. G., & Major, J., 1977: Terrestrial vegetation of California. *Valley grassland. Wiley and Sons, New York*, 491-514.

Hulley, G., Luvall, J., Sismanidis, P., & Keramitsoglou, I., 2019a: A high spatio-temporal resolution land surface temperature (LST) product for urban environments, LCLUC team meeting, Rockville, MD, 2019a, https://lcluc.umd.edu/sites/default/files/lcluc_documents/Hulley_LCLUC2019_Urban_LST.pdf

Hulley, G., Shivers, S., Wetherley, E., & Cudd, R., 2019b: New ECOSTRESS and MODIS Land Surface Temperature Data Reveal Fine-Scale Heat Vulnerability in Cities: A Case Study for Los Angeles County, California. *Remote Sensing, 11*

Hulley, G.C., Gottsche, F., Rivera, G., Hook, S., Freepartner, R., Radocinksi, R., Martin, M., Cawse-Nicholson, K., & Johnson, W.R., 2021: Validation and quality assessment of the ECOSTRESS level-2 land surface temperature and emissivity product. *IEEE Transactions on Geoscience and Remote Sensing, 1-23.*

Gately, C.K. and L.R. Hutyra, 2017: Large uncertainties in urban-scale carbon emissions. *Journal of Geophysical Research – Atmospheres*, 122: 11,242-11260.

Hutyra, L. R., Duren, R., Gurney, K. R., Grimm, N., Kort, E. A., Larson, E., & Shrestha, G., 2014: Urbanization and the carbon cycle: Current capabilities and research outlook from the natural sciences perspective. *Earth's Future*, *2*(10), 473–495.

Madani, N., Kimball, J. S., Jones, L. A., Parazoo, N. C., & Guan, K. (2017). Global analysis of bioclimatic controls on ecosystem productivity using satellite observations of solar-induced chlorophyll fluorescence. *Remote Sensing*, *9*(6). https://doi.org/10.3390/rs9060530

Madani, N., Parazoo, N. C., Kimball, J. S., Ballantyne, A. P., Reichle, R. H., Maneta, M., … Tagesson, T. (2020). Recent Amplified Global Gross Primary Productivity Due to Temperature Increase Is Offset by Reduced Productivity Due to Water Constraints. *AGU Advances*, *1*(4). https://doi.org/10.1029/2020av000180

Mahadevan, P., Wofsy, S. C., Matross, D. M., Xiao, X., Dunn, A. L., Lin, J. C., … Gottlieb, E. W. 2008: A satellite-based biosphere parameterization for net ecosystem CO_2exchange: Vegetation Photosynthesis and Respiration Model (VPRM). *Global Biogeochemical Cycles*, *22*(2).

Miller, J. M, S J Lehman, K Verhulst, E. Miller, R Duren, V Yadav, S Newman, C Sloop, 2020: Large and seasonally varying biospheric CO_2 fluxes in the Los Angeles megacity revealed by atmospheric radiocarbon: *Proceedings of the National Academy of Science*, 117(43), pp.26681-26687.

Miller, D.L., Alonzo, M., Roberts, D.A., Tague, C.L. and McFadden, J.P., 2020: Drought response of urban trees and turfgrass using airborne imaging spectroscopy. *Remote Sensing of Environment*, *240*, p.111646.

Mishra, V., Ganguly, A.R., Nijssen, B. and Lettenmaier, D.P., 2015: Changes in observed climate extremes in global urban areas. *Environmental Research Letters*, *10*(2), p.024005.

Park, C., Gerbig, C., Newman, S., Ahmadov, R., Feng, S., Gurney, K. R., … Ryerson, T., 2018: CO_2 transport, variability, and budget over the Southern California Air Basin using the high-resolution WRF-VPRM model during the CalNex 2010 campaign. *Journal of Applied Meteorology and Climatology*, *57*(6), 1337–1352.

Petri, A. C., Koeser, A. K., Lovell, S. T., & Ingram, D., 2016: How Green Are Trees? — Using Life Cycle Assessment Methods to Assess Net Environmental Benefits. *Journal of Environmental Horticulture*, *34*(4), 101–110.

Reinmann, A. B., & Hutyra, L. R., 2017: Edge effects enhance carbon uptake and its vulnerability to climate change in temperate broadleaf forests. *Proceedings of the National Academy of Sciences*, *114*(1), 107–112.

Reinmann, A. B., I. A. Smith, J. R. Thompson, and L. R. Hutyra, 2020: Urbanization and fragmentation mediate temperate forest carbon cycle response to climate, *Environmental Research Letters*, 15(11), 114036.

Sargent, M., Barrera, Y., Nehrkorn, T., Hutyra, L. R., Gately, C. K., Jones, T., McKain, K., Sweeney, C., Hegarty, J., Hardiman, B. et al., 2018: Anthropogenic and biogenic CO2 fluxes in the Boston urban region, *Proceedings of the National Academy of Sciences*, 115(29), 7491–7496.

Schneider, F. D., Morsdorf, F., Schmid, B., Petchey, O. L., Hueni, A., Schimel, D. S., & Schaepman, M. E., 2017: Mapping functional diversity from remotely sensed morphological and physiological forest traits. *Nature Communications*, *8*(1), 1441.

Seto, K.C.; Güneralp, B.; Hutyra, L.R., 2012: Global forecasts of urban expansion to 2030 and direct impacts on biodiversity and carbon pools, *Proceedings of the National Academy of Sciences,* USA, 109, 16083–16088

Smith, I. A., Dearborn, V. K., & Hutyra, L. R., 2019: Live fast, die young: Accelerated growth, mortality, and turnover in street trees. *PLoS ONE*, *14*(5), 1–17.

Stovall, A. E. L., Shugart, H., & Yang, X., 2019: Tree height explains mortality risk during an intense drought. *Nature Communications*, *10*(1), 1–6.

Strohbach, M.W., Arnold, E. and Haase, D., 2012: The carbon footprint of urban green space—A life cycle approach. *Landscape and Urban Planning*, *104*(2), pp.220-229.

Turnbull, J. C., Sweeney, C., Karion, A., Newberger, T., Lehman, S. J., Tans, P. P., Davis, K. J., Lauvaux, T., Miles, N. L., Richardson, S. J., Cambaliza, M. O., Shepson, P. B., Gurney, K., Patarasuk, R. and Razlivanov, I., 2015: Toward quantification and source sector identification of fossil fuel CO_2 emissions from an urban area: Results from the INFLUX experiment, *J. Geophys. Res.*, 120(1), 292–312.

Turner, A. J., Köhler, P., Magney, T. S., Frankenberg, C., Fung, I., & Cohen, R. C., 2020:. A double peak in the seasonality of California's photosynthesis as observed from space. *Biogeosciences*, *17*(2), 405–422.

Underwood, E. C., Ustin, S. L., & Ramirez, C. M., 2007: A Comparison of Spatial and Spectral Image Resolution for Mapping Invasive Plants in Coastal California. *Environmental Management*, *39*(1), 63–83.

United Nations, 2012: World urbanization prospects, the 2011 revision: Highlights, United Nations Department of economic and social affairs, Population Division, New York, NY. Retrieved from www.un.org/en/development/desa/publications/ world-urbanization-prospects-the-2011-revision.html.

Vo, T. T., & Hu, L., 2021: Diurnal evolution of urban tree temperature at a city scale. *Scientific Reports*, *11*(1), 1–13.

Wang, Z., Chlus, A., Geygan, R., Ye, Z., Zheng, T., Singh, A., et al., 2020: Foliar functional traits from imaging spectroscopy across biomes in eastern North America. *New Phytologist*, *228*(2), 494–511. https://doi.org/10.1111/nph.16711

Wetherley, E. B., McFadden, J. P., & Roberts, D. A., 2018: Megacity-scale analysis of urban vegetation temperatures. *Remote Sensing of Environment*, *213*, 18-33.

Wu, D., Lin, J. C., Duarte, H. F., Yadav, V., Parazoo, N. C., Oda, T., and Kort, E. A., 2021: A Model for Urban Biogenic CO_2 Fluxes: Solar-Induced Fluorescence for Modeling Urban biogenic Fluxes (SMUrF v1), *Geosci. Model Dev.*, 14(16), 3633-3661.

Yadav, V., R. Duren, K. Mueller, K. R. Verhulst, T. Nehrkorn, J. Kim, et al., 2019: Spatio-temporally Resolved Methane Fluxes From the Los Angeles Megacity, *Journal of Geophysical Research: Atmospheres*, 124(9), 5131-5148.

Yadav, J, S. Ghosh, K. Mueller, A. Karion, G. Roest, S. Gourdji, I. Lopez-Coto, K. Gurney, K. Verhlust, N. C. Parazoo, J. Kim, M. Stock, E. DiGangi, S. Prinzivalli, C. Fain, R. Keeling, R. Weiss, R. Duren, J Henderson, C. Miller, J. Whetstone, 2021: The impact of COVID-19 on CO2 emissions in the Los Angeles and Washington DC/Baltimore metropolitan areas, *Geophysical Research Letters*, 48(11), 1-10.

Ye, X., Lauvaux, T., Kort, E. A., Oda, T., Feng, S., Lin, J. C., Yang, E. G. and Wu, D. 2020: Constraining fossil fuel CO_2 emissions from urban area using OCO-2 observations of total column CO_2, J. *Geophys. Res. Atmos.*, 125(8), e2019JD030528.

Zhang, Y., Joiner, J., Hamed Alemohammad, S., Zhou, S., & Gentine, P., 2018: A global spatially contiguous solar-induced fluorescence (CSIF) dataset using neural networks. *Biogeosciences*, *15*(19), 5779–5800.

Figure Captions

Figure 1. Maps showing geographic complexity of study region in terms of topography and land surface characteristics. (A) Study region encompasses Los Angeles urban region (red shading) and the greater Southern California Air Basin (SoCAB) (grey). (B) Urban region is surrounding by diverse topographic features. (C) Vegetated and non-vegetated land cover is derived from National Airborne Inventory Program (NAIP) and Sentinel-2 Imagery (Coleman et al., 2020a). (D) Irrigation fraction is derived from high resolution land cover, ECOSTRESS thermal data, and Landsat imagery (Coleman et al., 2020b). (E) Landscape fragmentation, including edge and interior vegetation and urban greenspace, is derived using algorithms from Reinmann and Hutyra (2017). (F) Gross primary production (GPP) is derived from the UrbanVPRM carbon cycle model, constrained by vegetation remote sensing, meteorological reanalysis, and tower optimized vegetation parameters (characterizing sensitivity to temperature and sunlight). Each pixel is 30 m^2 in area.

Figure 2. The annual cycle of GPP across SoCAB (solid) differs substantially in the timing and magnitude of peak GPP for urban (dotted) and non-urban (dashed) regions. Results include vegetated surfaces only (grass, tree, or shrub). Spatially and temporally averaged GPP, representing monthly mean productivity per unit vegetated area, is shown in (a). Spatially and monthly integrated values, represented integrated GPP over all vegetated surfaces, is shown in (b). The green lines show a proxy of based on estimates of Solar Induced Fluorescence from the Contiguous SIF (CSIF) product (Zhang et al., 2018), scaled by a factor of 20 to show relative seasonal variability. Urban region corresponds to red shaded in region in **Fig 1a**.

Figure 3. Similar vegetation types have different influences on the annual GPP cycle in non-urban (left) and urban (right) regions. Vegetation classes include tree (dark green), grass (light green), and shrub (magenta), corresponding to the map in **Fig 1c**. Mean and cumulative GPP values are shown in the top and bottom rows, respectively (**see Fig 2**). Note that scale is reduced by a factor of four for urban GPP for visualization. Shaded areas in Figs 3-5 represent monthly confidence intervals derived from ANOVA of landcover groups, and calculated from the Tukey-Kramer method. This

Figure 4. The annual cycle of urban GPP is highly variable across managed and fragmented vegetation. Managed refers to irrigated or non-irrigated, and fragmentation to edge or interior. Monthly GPP is shown here as a function of irrigation (left), fragmentation (middle), and the combination of irrigation and edges (right). Mean and cumulative GPP values are shown in the top and bottom rows, respectively (**see Fig 2**).

Figure 5. Irrigation and edge effects on the annual cycle of GPP depends on vegetation type. Here, GPP is plotted as a function of land cover, irrigation, and landscape fragmentation. Individual effects of irrigation are shown in (a) and (d), of fragmentation in (b) and (e). Combined effects of land use on edge vegetation are shown in (c) and (f). Land use effects on interior vegetation not shown due to small sample size.

Tables

Table 1. Estimates of GPP from UrbanVPRM as a function of season, land cover (ISA, Tree, Grass, Shrub, NPV), land use (irrigated or non-irrigated), and fragmentation (interior or edge). Vegetated surfaces (Veg) refer to land cover classified as tree, grass, or shrub. Total refers to spatially and temporally integrated GPP. Mean refers to spatially and temporally averaged GPP (total GPP divided by area and time). The first and second values in each cell refer to SoCAB and Urban regions (grey and red regions in Fig 1a, respectively).

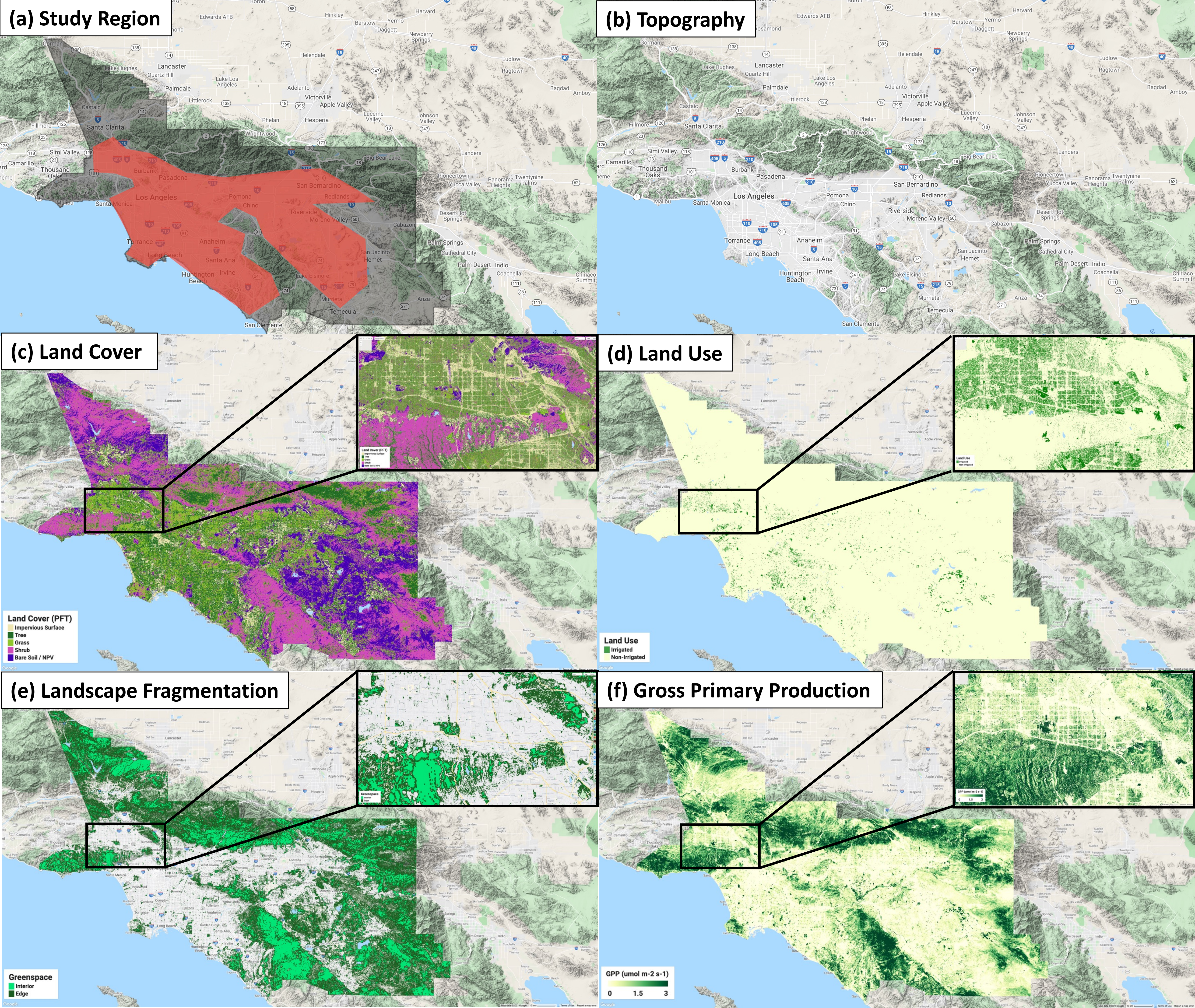
(a) Study Region
(b) Topography
(c) Land Cover
Land Cover (PFT)
Impervious Surface
Tree
Grass
Shrub
Bare Soil / NPV
(d) Land Use
Land Use
Irrigated
Non-Irrigated
(e) Landscape Fragmentation
Greenspace
Interior
Edge
(f) Gross Primary Production
GPP (umol m-2 s-1)
0
1.5
3

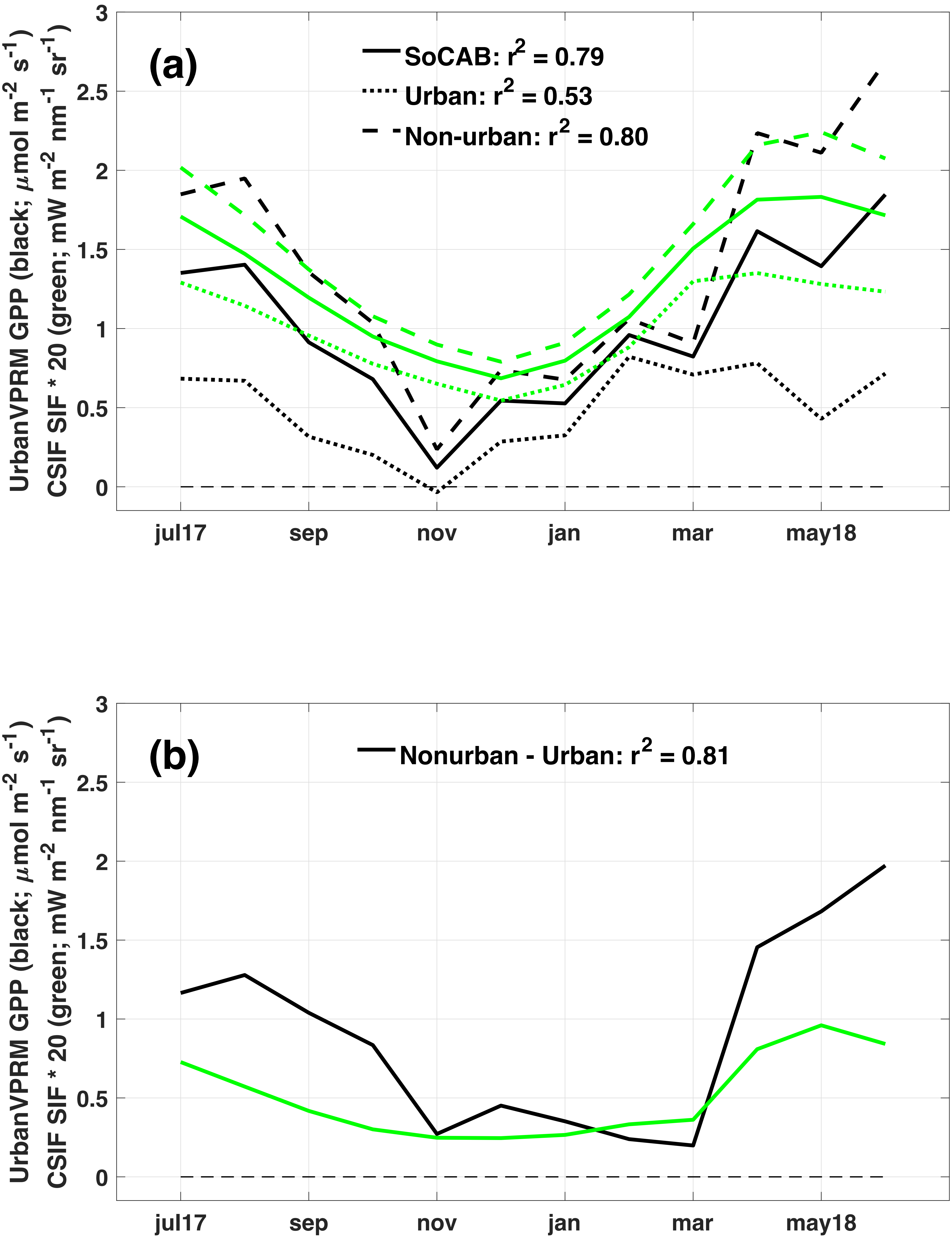

(a)
SoCAB: r^2 = 0.79
Urban: r^2 = 0.53
Non-urban: r^2 = 0.80
UrbanVPRM GPP (black; μmol m^-2 s^-1)
CSIF SIF * 20 (green; mW m^-2 nm^-1 sr^-1)
0
0.5
1
1.5
2
2.5
3
jul17
sep
nov
jan
mar
may18
(b)
Nonurban - Urban: r^2 = 0.81
UrbanVPRM GPP (black; μmol m^-2 s^-1)
CSIF SIF * 20 (green; mW m^-2 nm^-1 sr^-1)
0
0.5
1
1.5
2
2.5
3
jul17
sep
nov
jan
mar
may18

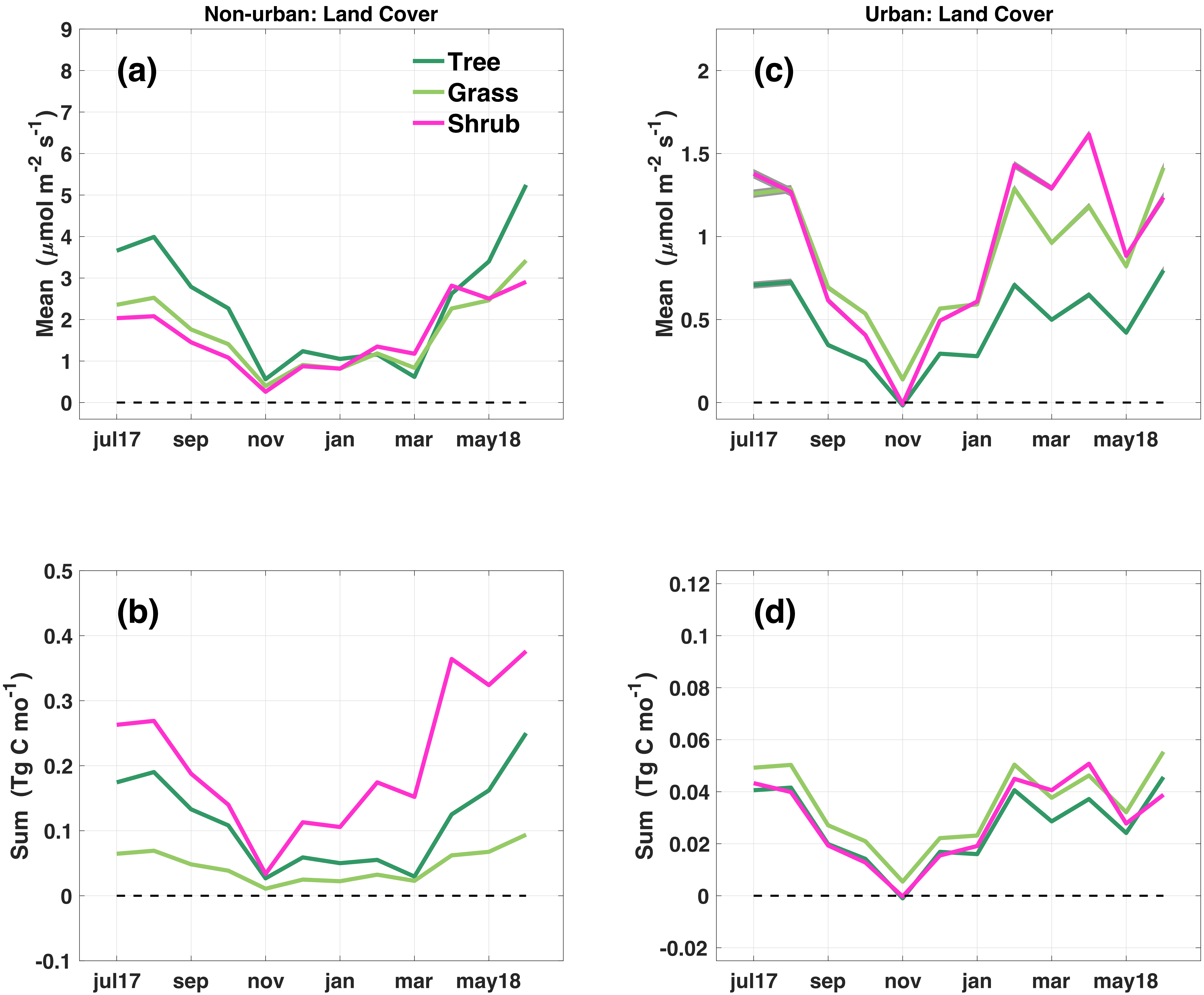

Non-urban: Land Cover
Urban: Land Cover
(a)
(b)
(c)
(d)
Tree
Grass
Shrub
Mean (μmol m^{-2} s^{-1})
Sum (Tg C mo^{-1})
jul17
sep
nov
jan
mar
may18

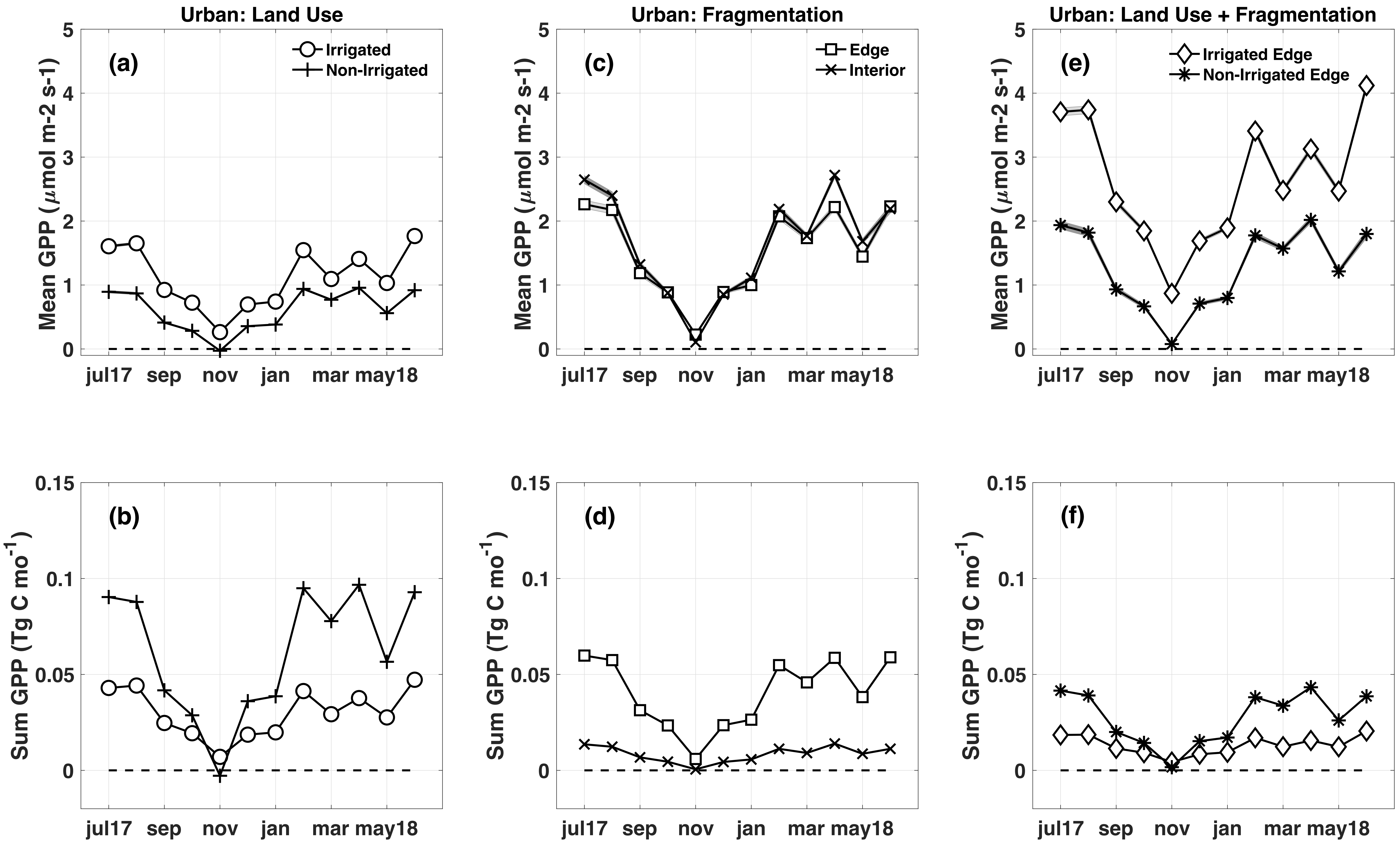
Urban: Land Use
Urban: Fragmentation
Urban: Land Use + Fragmentation
(a)
(b)
(c)
(d)
(e)
(f)
Irrigated
Non-Irrigated
Edge
Interior
Irrigated Edge
Non-Irrigated Edge
Mean GPP (μmol m-2 s-1)
Sum GPP (Tg C mo^{-1})
0
1
2
3
4
5
0
0.05
0.1
0.15
jul17
sep
nov
jan
mar
may18

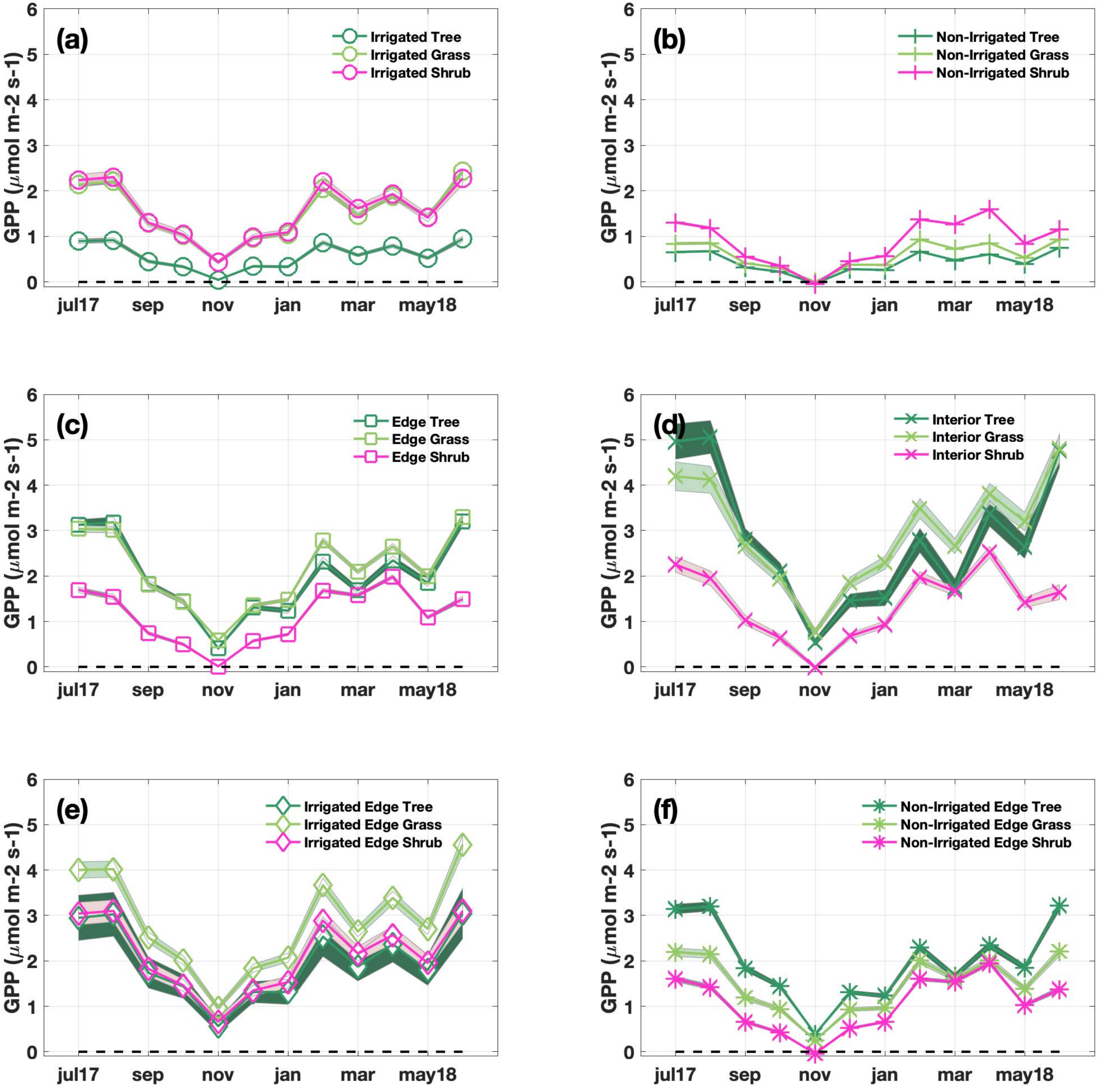

(a)
Irrigated Tree
Irrigated Grass
Irrigated Shrub
(b)
Non-Irrigated Tree
Non-Irrigated Grass
Non-Irrigated Shrub
(c)
Edge Tree
Edge Grass
Edge Shrub
(d)
Interior Tree
Interior Grass
Interior Shrub
(e)
Irrigated Edge Tree
Irrigated Edge Grass
Irrigated Edge Shrub
(f)
Non-Irrigated Edge Tree
Non-Irrigated Edge Grass
Non-Irrigated Edge Shrub
GPP (μmol m-2 s-1)
0
1
2
3
4
5
6
jul17
sep
nov
jan
mar
may18

	Area (km^2)	Gross Primary Production: SoCAB (Urban)					
		Total (Tg C)			Mean (μmol m^{-2} s^{-1})		
		Spring (MAM)	Summer (JJA)	Annual	Spring (MAM)	Summer (JJA)	Annual
All	16165 (6893)	2.02 (0.45)	2.43 (0.49)	6.47 (1.38)	1.29 (0.67)	1.55 (0.71)	0.99 (0.52)
Veg	10694 (4114)	1.69 (0.34)	2.24 (0.43)	5.73 (1.15)	1.64 (0.86)	2.16 (1.07)	1.38 (0.73)
Tree	3378 (1844)	0.43 (0.09)	0.79 (0.14)	1.80 (0.34)	1.29 (0.53)	2.36 (0.77)	1.34 (0.49)
Grass	2142 (1259)	0.28 (0.12)	0.40 (0.16)	1.02 (0.44)	1.35 (0.99)	1.93 (1.32)	1.23 (0.90)
Shrub	5174 (1011)	0.98 (0.13)	1.05 (0.13)	2.93 (0.37)	2.00 (1.29)	2.14 (1.32)	1.48 (0.96)
Irrigated	(860)	(0.11)	(0.13)	(0.36)	(1.35)	(1.67)	(1.12)
Non-Irr	(3250)	(0.27)	(0.27)	(0.74)	(0.89)	(0.89)	(0.61)
Interior	(165)	(0.03)	(0.04)	(0.10)	(2.22)	(2.41)	(1.65)
Edge	(850)	(0.16)	(0.18)	(0.48)	(2.00)	(2.22)	(1.52)
Irrigated Edge	(160)	(0.04)	(0.06)	(0.16)	(3.00)	(3.86)	(2.64)

Non-Irr Edge	(690)	(0.11)	(0.12)	(0.33)	(1.79)	(1.85)	(1.28)

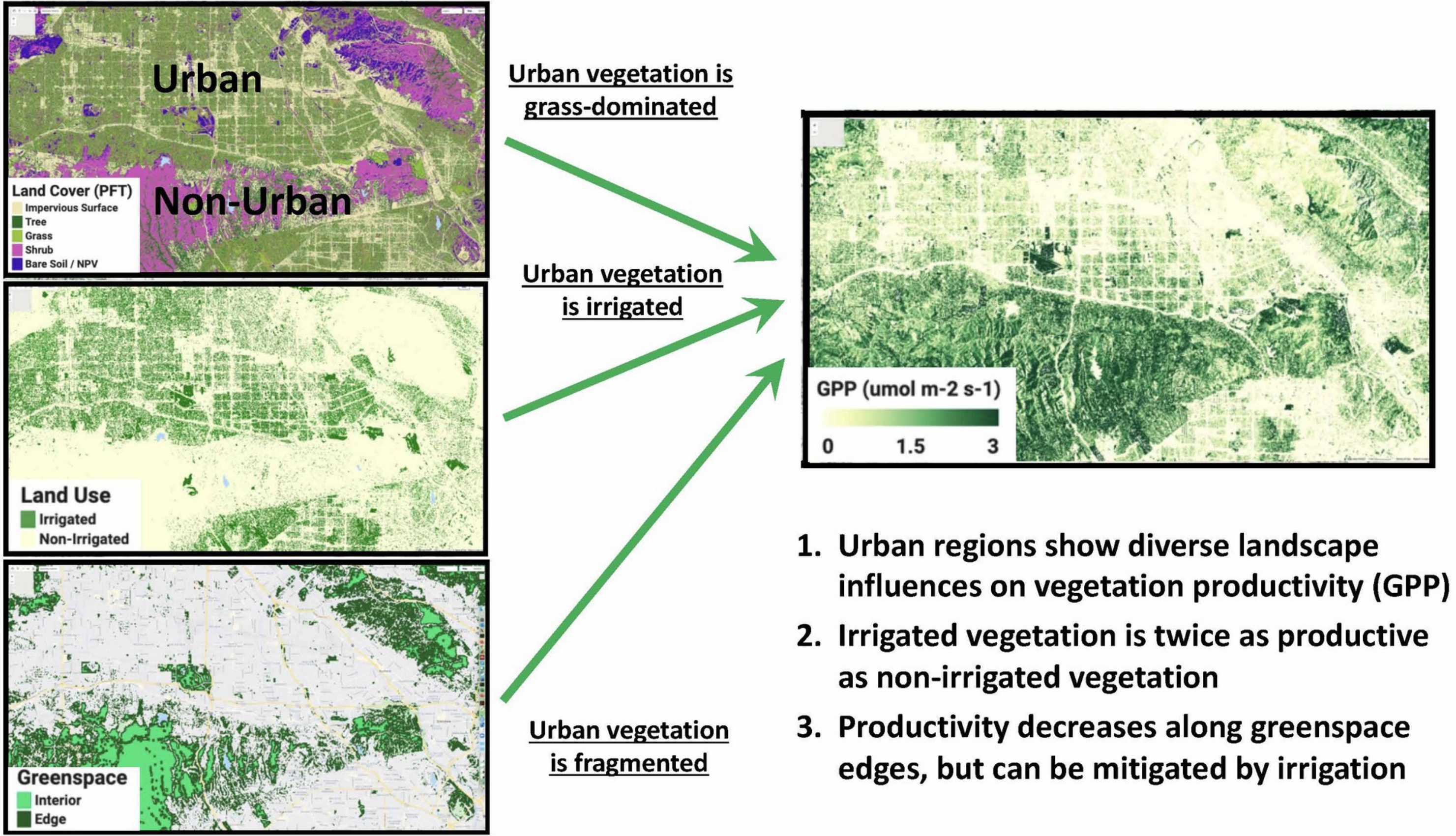
Urban
Non-Urban
Land Cover (PFT)
Impervious Surface
Tree
Grass
Shrub
Bare Soil / NPV
Land Use
Irrigated
Non-Irrigated
Greenspace
Interior
Edge
Urban vegetation is grass-dominated
Urban vegetation is irrigated
Urban vegetation is fragmented
GPP (umol m-2 s-1)
0
1.5
3
1. Urban regions show diverse landscape influences on vegetation productivity (GPP)
2. Irrigated vegetation is twice as productive as non-irrigated vegetation
3. Productivity decreases along greenspace edges, but can be mitigated by irrigation